Mechanistic insight into the adsorption and photocatalytic activity of a magnetically separable

by Arif Hidayat

Submission date: 29-Mar-2023 06:09AM (UTC+0700)
Submission ID: 2049439126
File name: 1MECHA_1.PDF (6.78M)
Word count: 7286
Character count: 38961

Chemical Physics Letters 792 (2022) 139410

Contents lists available at ScienceDirect

Chemical Physics Letters

journal homepage: www.elsevier.com/locate/cplett

Mechanistic insight into the adsorption and photocatalytic activity of a magnetically separable γ-Fe_2O_3/Montmorillonite nanocomposite for rhodamine B removal

Is Fatimah [a,*], Gani Purwiandono [a], Arif Hidayat [b], Suresh Sagadevan [c], Azlan Kamari [d]

[a] Department of Chemistry, Faculty of Mathematics and Natural Sciences, Universitas Islam Indonesia, Kampus Terpadu UII, Jl. Kaliurang Km 14, Sleman, Yogyakarta, Indonesia
[b] Department of Chemical Engineering, Faculty of Industrial Technology, Universitas Islam Indonesia, Kampus Terpadu UII, Jl. Kaliurang Km 14, Sleman, Yogyakarta, Indonesia
[c] Nanotechnology and Catalysis Research Center, University Malaya, Malaysia
[d] Chemistry Department, Universiti Pendidikan Sultan Idris Perak, Perak 35900, Malaysia

ARTICLE INFO

Keywords:
Adsorption
Clay
Magnetic
Photocatalytic

ABSTRACT

The magnetically separable nanocomposite of γ-Fe_2O_3/montmorillonite (γ-Fe_2O_3/Mt) has been synthesized by a hydrothermal method. The as-obtained nanocomposite is composed of a single phase of γ-Fe_2O_3 nanoparticles homogeneously dispersed in a montmorillonite structure with high photocatalytic activity for rhodamine B photodegradation. Physicochemical characterization revealed particle sizes ranging from 10 to 30 nm with a band-gap energy of 2.3 eV. This study reveals a significant contribution of the adsorption mechanism to the degradation mechanism. The nanocomposite could be easily separated and reused by magnetic separation owing to its magnetism of 22 emu/g. The nanocomposite is also reusable without any chemical change until five cycles.

1. Introduction

Organic compound-containing wastewater is a serious problem in many industries that require emerging technology for removal. The persistence properties of organic compounds bring potential damage to aquatic environments and cause the accumulation of vast environmental problems, which must raise concerns before allowing their discharge to the environment [1,2]. Organic compounds classified as dyes, especially azo dyes, are considered serious and harmful contaminants characterized as biologically toxic (carcinogenic, mutagenic, and teratogenic), irritants, and infectious. The textile, printing, paint, and pharmaceutical industries highly consume these dye compounds; unfortunately, more than 15% of the consumed amount is discharged into wastewater [3]. Evidently, these dyes are the major pollutants from many industries and are clearly major hazards to groundwater. Rhodamine B (RhB) is a significant and well-known basic xanthene dye that is a major ingredient in the above-mentioned industries. The discharge of RhB-containing wastewater is a serious threat to the environment, even at low concentrations in water; thus, it is a representative target organic pollutant for photocatalytic efficiency examination.

Heterogeneous photocatalytic oxidation, as part of the advanced oxidation process (AOPs), has proven to be a promising technology for organic-containing water. Its removal mechanism, which includes oxidation, for the target compound is advantageous over the use of adsorption technologies [4,5]. The method depends on the photocatalytic activity of semiconductor photocatalysts, and its reusability and recyclability are value-added characteristics of the technology.

Adsorption capability, stability, easy separation, and high photoactivity in the visible range are the significant properties required for materials to be used as photocatalysts [6]. Recent studies showed that adsorption capability of the photocatalyst is the important function in photocatalysis mechanism, and based on this, semiconductor immobilized onto porous material is ideal for the mechanism due to the surface area availability [7,8]. The development of nanomaterials with magnetic photocatalysts involves a combination of these properties and has been described as an efficient method for improving the effectiveness of the photocatalytic oxidation process [9–11]. Iron oxide-based magnetic nanoparticles are well known magnetically separable materials, and their combination with supportive solids with high porosity and chemical stability has received great attention. α-Fe_2O_3, γ-Fe_2O_3, and Fe_3O_4

* Corresponding author.
E-mail address: isfatimah@uii.ac.id (I. Fatimah).

https://doi.org/10.1016/j.cplett.2022.139410
Received 8 October 2021; Received in revised form 21 January 2022; Accepted 23 January 2022
Available online 29 January 2022

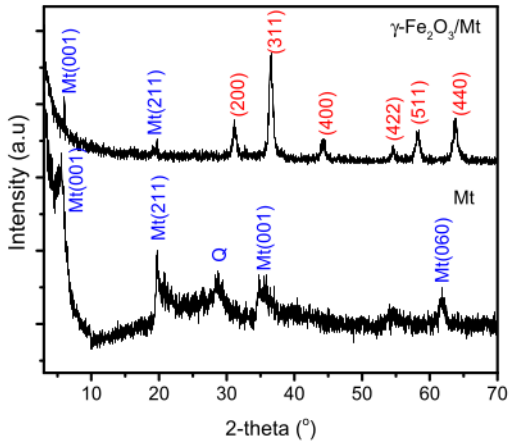

Fig. 1. XRD pattern of materials.

have been widely studied as magnetic active nanoparticles; within this scheme, nanocomposite development using silica-, carbon-, and clay-based materials has been attempted [12]. The swelling capability and modifiable properties of their chemical structures cause clay materials to produce homogeneously distributed magnetic nanoparticles. Surface properties potentially contribute to this activity via an adsorption mechanism [13–15]. In this work, dispersed γ-Fe_2O_3 nanoparticles in montmorillonite (Mt) clay support were prepared. The aim of the present work was to determine the characteristics of materials and the photocatalytic features for the photocatalytic degradation of RhB in aqueous solutions as a model pollutant. In addition, this study provides mechanistic insight into adsorption and photocatalytic properties, especially with magnetically separable characteristics.

2. Materials and methods

2.1. Materials

The Mt used in this work was obtained from Pacitan, East Java, Indonesia. The material was previously washed with water, dried in an oven, and ground to a size of 200 mesh before use. The cation exchange capacity of the material was 69 meq/g. Chemicals consisting of $FeCl_3$, RhB, NaOH, ethylene diamine tetra acetate (EDTA), isopropanol, and H_2O_2 were purchased from Merck (Darmstadt, Germany).

2.2. Preparation of nanocomposites

First, dispersed γ-Fe_2O_3 nanoparticles in Mt (γ-Fe_2O_3/Mt) was prepared using a Mt suspension, by dissolving Mt powder in water at a concentration of 10% wt. An iron oxide precursor was prepared, referring to the previous syntheses of γ-Fe_2O_3 nanoparticles (γ-Fe_2O_3 NPs) by dissolving $FeCl_3{\cdot}6H_2O$ and $FeSO_4{\cdot}7H_2O$ with a Fe^{3+}/Fe^{2+} molar ratio of 2:1 in double distilled water [16]. The precursor solution was continuously stirred before it was mixed with the Mt suspension at a theoretical percentage of Fe of 10% wt, followed by stirring for 1 h. Into the mixture, the NaOH solution was added slowly and then poured into a Teflon-lined autoclave and kept at 150 °C overnight. The obtained precipitate was dried in an oven at 100 °C and further calcined at 200 °C for 4 h to obtain powder samples, which were designated as γ-Fe_2O_3/Mt.

For comparison, γ-Fe_2O_3 was also synthesized using the same precursor, hydrothermal treatment condition, and calcination temperature with the synthesis of γ-Fe_2O_3/Mt, but without dispersion into a clay suspension.

2.3. Material characterization

The physicochemical properties of the samples were characterized using field emission-scanning electron microscopy (FE-SEM), transmission electron microscopy (TEM), X-ray diffraction (XRD), X-ray photoelectron spectroscopy (XPS), gas sorption analysis, ultraviolet diffuse reflectance spectrophotometry (UV-DRS), and Fourier transform infrared. A Phenom X instrument (US) was used for SEM analysis, while TEM images were taken using a JEOL TEM 2010 transition electron microscope operated at an applied voltage of 200 kV. The XRD of XPERT-PRO with a Ni-filtered Cu Kα radiation (λ = 0.154060 nm) was used for analysis at a range of 2–70°. The Thermo Nicolet Avatar system (Madison, USA) was used to examine the changes in the surface functional groups of the materials, while the XPS was performed on a V.G. Scientific ESKALAB MKII instrument. Monochromatic Al K_α radiation with a photon energy of 1486.6 ± 0.2 eV was used for analyses. Before analysis, approximately 0.2 mg of sample was slightly pressed into a small pellet of 15 mm in diameter and then mounted on the sample holder for degassing for 4 h to achieve a dynamic vacuum of $< 10^{-8}$ Pa. A vibration sample magnetometer (VSM)-BHV-5 (Japan) was used for the magnetism of the composite.

2.4. Adsorption and photocatalytic experiments

The adsorption experiments were conducted in a batch adsorption system using a horizontal shaker. The experimental setup for the photocatalytic activity measurements included a 40-W xenon lamp-

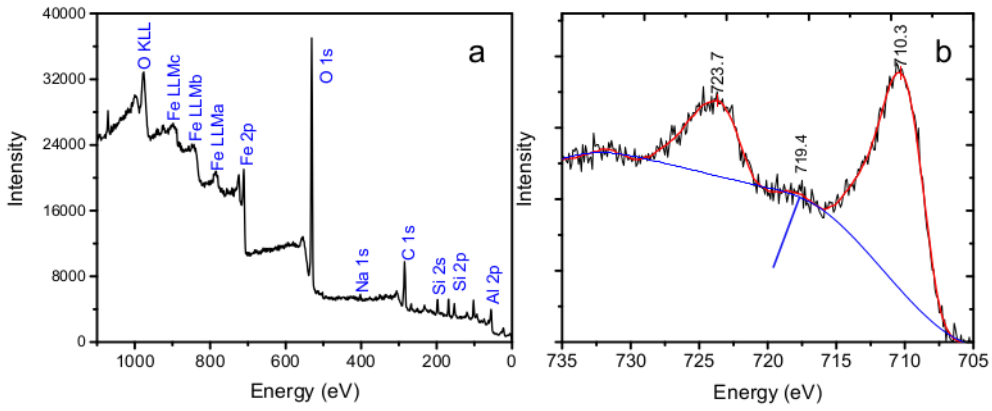

Fig. 2. XPS spectra of γ-Fe_2O_3 /Mt (a) survey scan (b) Fe 2p spectrum.

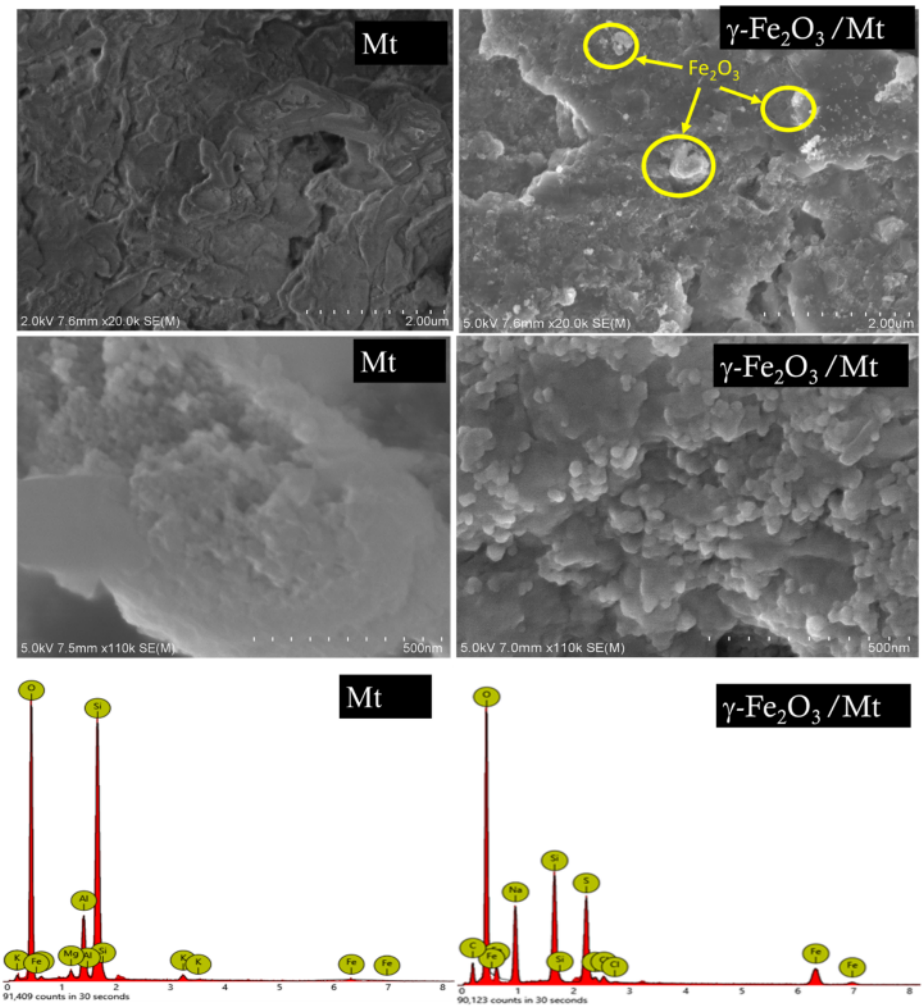

Fig. 3. SEM-EDX of materials.

equipped batch photoreactor. The entire photoreactor system was maintained at room temperature using a water cooler. For each photocatalytic activity test, the photocatalyst powder was mixed with the dye solution with stirring and light exposure. Samples from the adsorption and photocatalytic activity tests were collected at a certain time, and the RhB concentration was determined using the colorimetric method with a 1 2010 UV–visible spectrophotometer (Hitachi, Singapore). The degradation efficiency (DE; %) in the photocatalytic activity test was calculated using Eq. (1).

$$\mathrm{DE}(\%) = \frac{C_0 - C_t}{C_0} x100 \quad (1)$$

where C_o and C_t are the initial RhB concentration and concentration of RhB at the sampling time t.

To ensure the degradation mechanism, experiments on effect of scavenger to the kinetics of RhB degradation was also performed. High performance liquid chromatography (HPLC) on Agilent 1260 (Singapore) was employed for analysis. Analysis was performed on the condition: analytical C81 column as stationary phase, mobile phase of acetonitrile:phosphate buffer pH 3.5 (1:1), ambient temperature (28–32 °C), flow rate 1.2 mL/min.

3. Results and discussion

3.1. Material characterization

Physically, γ-Fe_2O_3/Mt was prepared in the form of black powder and easily attracted by the magnet field. Fig. 1 shows the XRD profile of the materials. The Mt sample demonstrated peaks associated with the structure at 5.59°, 19.69°, and 34.67°, which corresponded to the (001), (211), and (004) planes, respectively, referring to JCPDS 43–0688 [17]. γ-Fe_2O_3/Mt represents some peaks attributed to (220), (311), (400), (422), (511), and (440), which are in agreement with the values of the standard data (JCPDS no. 4–755) [18–21]. In addition, the (001) and (211) planes are still maintained in the same position, reflecting no such increase or decrease in the basal spacing d_{001} of the interlayer structure. The peak associated with quartz as an impurity disappeared. By using the Scherer formula for the (311) plane, the particle size of γ-Fe_2O_3 was estimated at approximately 23.6 nm [22].

The obtained single phase of γ-Fe_2O_3 in the composite was mainly related to the easy dispersion of Fe(III) ions within the interlayer space of Mt due to the cation exchange capacity of Mt. We can also conclude that the optimum sintering temperature for producing the γ-Fe_2O_3 phase

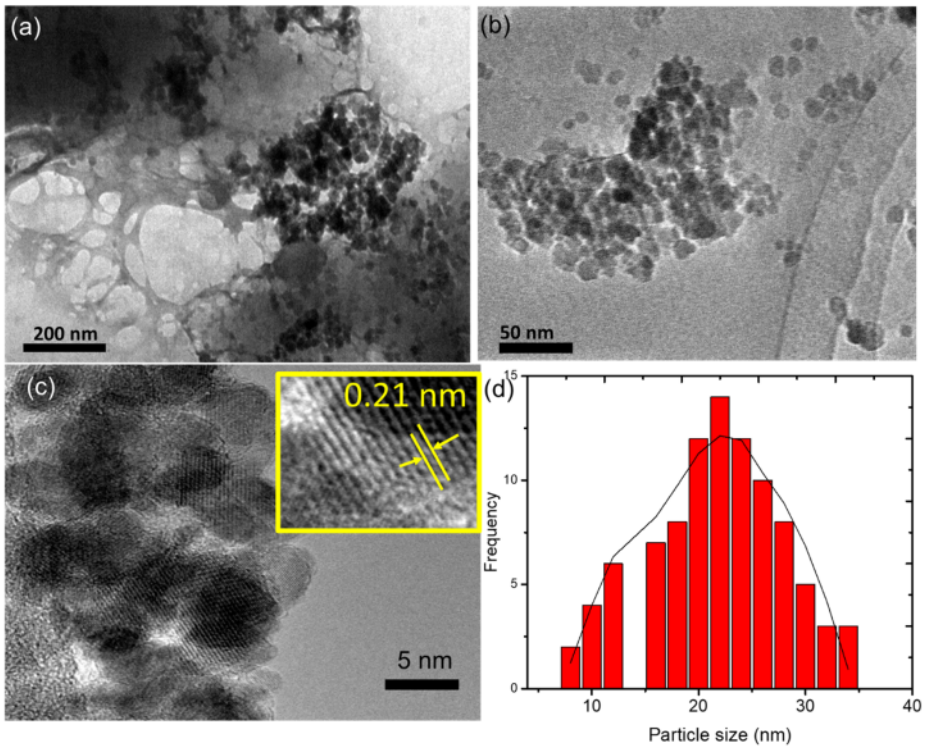

Fig. 4. (a-c) TEM image of γ-Fe_2O_3 /Mt (d) particle size distribution of γ-Fe_2O_3 in the composite.

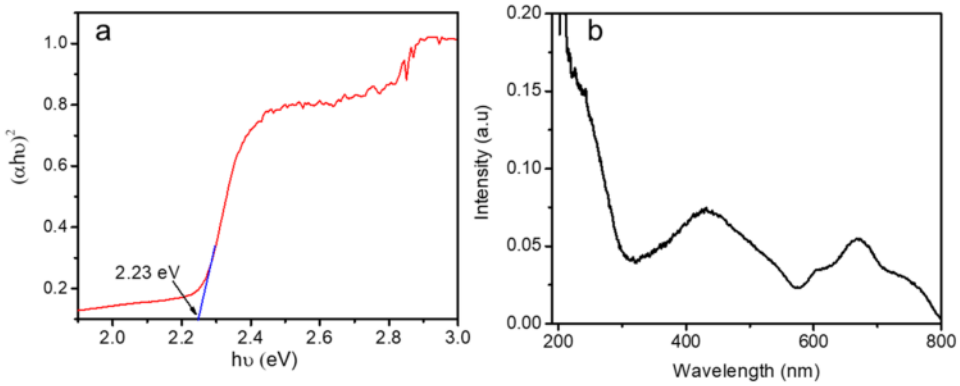

Fig. 5. (a) UV-DRS, and (b) PL spectrum spectrum of γ-Fe_2O_3 /Mt.

is 400 °C. Meanwhile, other possible phases such as Fe_3O_4, α-Fe_2O_3, and ε-Fe_2O_3 can be formed via the following reaction steps [23]:

$$Fe^{3+} + 3OH^- \Leftrightarrow Fe(OH)_{3(s)}$$

$$Fe(OH)_{3(s)} + H^+ + e^- \Leftrightarrow Fe_3O_{4(s)} + 5H_2O$$

$$2Fe_3O_4 + 1\,2\,O_2 \longrightarrow 3(\gamma - Fe_2O_3)$$

$$2Fe_3O_4 + 1\,2\,O_2 \longrightarrow 3(\alpha - Fe_2O_3)$$

The surface composition of γ-Fe_2O_3/Mt was further demonstrated using XPS with the spectra presented in Fig. 2. The survey scan represents some peaks attributed to Si, Al, O, and Fe, indicating the major composition of the composite. In addition, the low-intensity peak at 400 eV is the characteristic peak of Na 1 s, which is consistent with the naturally occurring Mt structure. The deconvolution of the Fe 2p spectra exhibits two appearing peaks at 723.7 and 710.3 eV, respectively, which are attributed to Fe $2p_{1/2}$ and Fe $2p_{3/2}$, respectively [24–27]. No signal or shoulder representing the presence of the Fe^{2+} ion, which usually exists at approximately 708 eV, was observed. This confirmed that the addition of the shakeup satellite peak occurred at 719.4 eV when no Fe^{2+} ion was found, consistent with the XRD pattern.

The effect of the γ-Fe_2O_3 nanoparticle dispersion on the morphology was investigated using FE-SEM. The SEM images in Fig. 3c depict different surface patterns in which γ-Fe_2O_3/Mt shows dispersed irregular forms of γ-Fe_2O_3 on the surface (as marked in the yellow dashed circles). With higher magnification, the rounded cubic and irregular

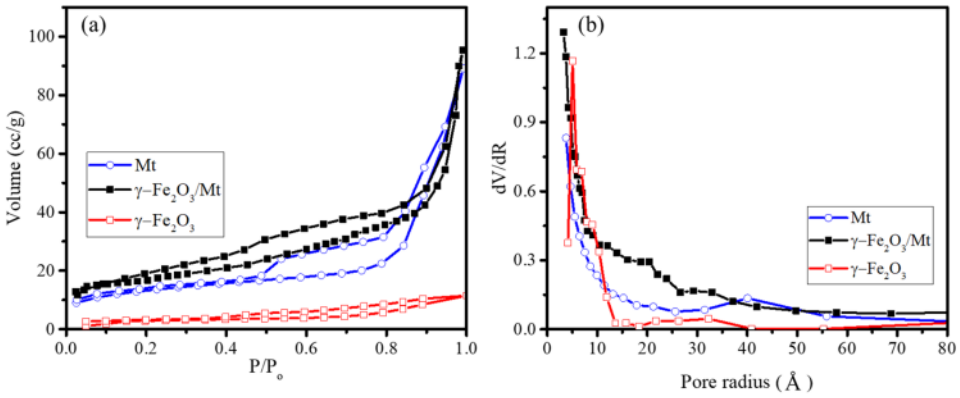

Fig. 6. a. Adsorption/desorption profile (b) Pore size distribution of γ-Fe_2O_3 /Mt in comparison with Mt and γ-Fe_2O_3.

spherical forms are confirmed. Further structural identification using TEM and high-resolution (HRTEM) revealed that the particle size ranged from 10 to 30 nm (Fig. 4d). These sizes are consistent with the calculated particle size from the XRD measurement, which was close to 23.6 nm on average. Furthermore, the HRTEM images of the irregular forms exhibited the distances of the adjacent lattice fringes, with an average of 0.21 nm, indicating agreement with the interplanar distance of the γ-Fe_2O_3(3 1 1) space, in reference to JCPDS, Ref. Code: 024-081 [25,28].

With respect to their photocatalytic application, the optical properties of the composites were identified using UV-DRS and photoluminescence spectrum measurements. The Tauc plot of photon energy ($h\nu$) against the $(\alpha h\nu)^2$ curve based on the Kubelka-Munk theory of materials is presented in Fig. 5. Conclusively, the plots show that the E_g of γ-Fe_2O_3/Mt is 2.23 eV. This value is higher than the band-gap values of γ-Fe_2O_3 nanoparticles that were reported in previous articles, in which the synthesized γ-Fe_2O_3 expressed a band gap of 2.03 eV [2228]. The increasing band-gap energy is related to the smaller particle size due to the quantum size effect and/or crystallite defect. A similar phenomenon was found in the dispersion of γ-Fe_2O_3 into porous Ni and in the composite of γ-Fe_2O_3/b-TiO_2 [29,30]. The narrow band-gap energy extends the photoresponse to visible-light and near-infrared regions, which is the benefit of the low-cost photocatalytic system [31,32].

Furthermore, the PL spectrum for γ-Fe_2O_3/Mt ranged from 350 to 700 nm (Fig. 5b). The excitation peaked at around 426 and 659 nm, and the peak at 659 nm was attributed to the 6A1 → 4 T1(4G) ligand field transition of Fe^{3+}. The data represent the condition that leads to the capability of composites to interact with photons in the UV and visible regions [33,34].

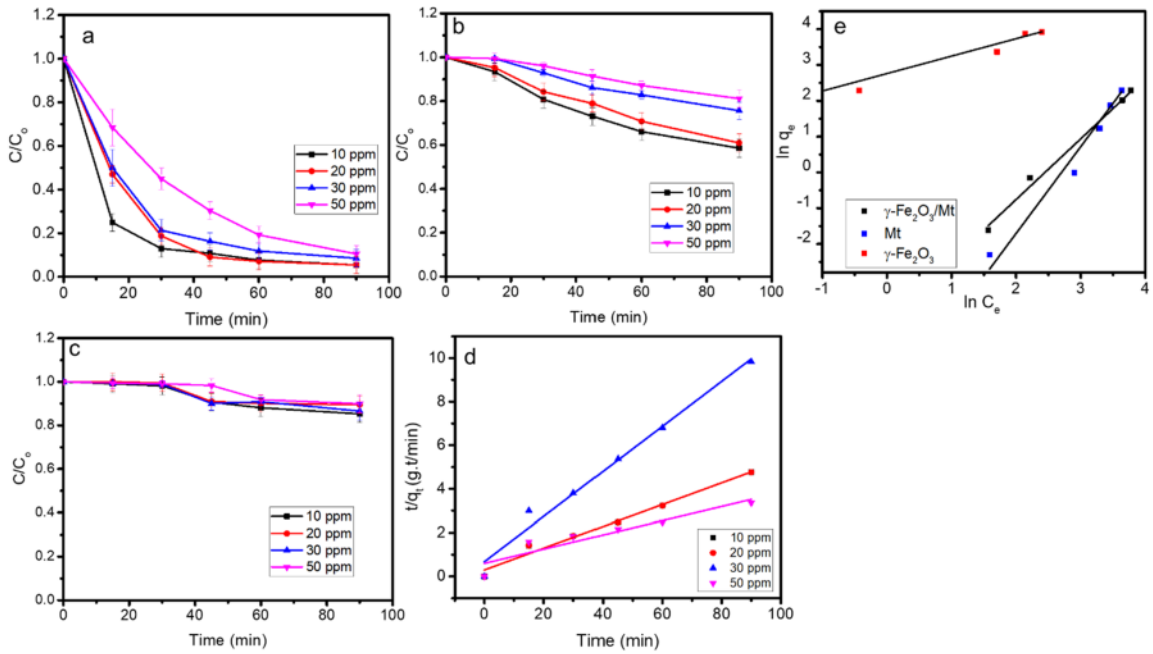

Fig. 7. (a). Kinetics of RhB adsorption using γ-Fe_2O_3 /Mt (b). Kinetics of RhB adsorption using Mt (c). Kinetics of RhB adsorption using γ-Fe_2O_3 (d) Pseudo-second order plots of RhB adsorption using γ-Fe_2O_3 /Mt (e). Freundlich isotherm plots of RhB adsorption using γ-Fe_2O_3 /Mt and Mt.

Table 1
calculated parameters from kinetics studies.

Pseudo-first-order			
	Kinetics parameter		
	R^2	k	Qe (mg/g)
γ-Fe_2O_3	0.897	1.06×10^{-3}	5.55
γ-Fe_2O_3 /Mt	0.944	2.55×10^{-2}	48.8
Mt	0.997	2.46×10^{-3}	15.4
Pseudo-second-order			
	R^2	**k**	**Qe**
γ-Fe_2O_3	0.977	1.18×10^{-3}	5.68
γ-Fe_2O_3 /Mt	0.997	2.08×10^{-2}	47.64
Mt	0.704	3.06×10^{-3}	9.86
Intra-particle diffusion			
	R^2	**k_i**	**C**
γ-Fe_2O_3	0.706	0.23	−0.48
γ-Fe_2O_3 /Mt	0.991	3.00	−0.35
Mt	0.900	0.60	−1.11

Table 2
Calculated isotherm parameters.

Adsorbent	Freundlich Isotherm parameters			Langmuir Isotherm Parameters			
	K_F (L/g)	1/n	R^2	q_m (mg/g)	K_L (L/mg)	R_L	R^2
γ-Fe_2O_3	0.65	0.67	0.977	7.89	4.1 x10^{-3}	0.971	0.974
γ-Fe_2O_3 /Mt	1153.70	0.39	0.995	45.08	7.8 x10^{-2}	0.999	0.965
Mt	418.29	0.45	0.991	26.23	3.8 x10^{-2}	0.991	0.973

Fig. 6 shows the adsorption–desorption profile of γ-Fe_2O_3/Mt in comparison with Mt and the compared pore distributions. The plots demonstrate the increasing adsorption capability of Mt after modification by γ-Fe_2O_3 dispersion. The calculated parameters based on the adsorption/desorption profile provided a specific surface area of 89.9 m^2/g in γ-Fe_2O_3/Mt, which is higher than that of Mt (79.9 m^2/g) and γ-Fe_2O_3 (24.6 m^2/g). The specific surface area of γ-Fe_2O_3 is similarly with was reported in other previous works [35,36]. In this case, Mt plays a role in supporting a specific surface area and porosity, which theoretically influences the adsorption mechanism. Similar phenomenon was also occurred in the dispersion of γ-Fe_2O_3 onto kaolinite [35]. The increasing surface area parameter is consistent with the profile in that the pore distribution also increased, mainly at the microporous structure. Based on the pore distribution pattern, which implied no change in dominant pores, the average diameters of the pores were not significantly different, 11.3 Å in Mt and 11.8 Å in γ-Fe_2O_3/Mt.

A similar pattern was reported in a previous work on the dispersion of Fe_3O_4 into Mt and the dispersion of SnO_2 nanoparticles [17,37]. The increasing specific surface area in the composite generally represents the homogeneous distribution of the dispersed materials.

3.2. Adsorption experiment

The adsorption experiments of RhB using γ-Fe_2O_3, γ-Fe_2O_3/Mt, and Mt were performed in a horizontal shaker at room temperature. The kinetics of RhB removal using γ-Fe_2O_3/Mt , Mt, and γ-Fe_2O_3 are presented in Fig. 7a-7c. The plots indicate the significant improvement in RhB removal by γ-Fe_2O_3/Mt compared with Mt and γ-Fe_2O_3. Basically, the increasing adsorption was related to the specific surface area enlarged by the composite formation. This was confirmed by the lower adsorption rate and capacity over γ-Fe_2O_3. The data showed that the kinetics of the adsorption was evaluated in accordance with Lagergren's pseudo-first order, Ho and McKay's pseudo-second order, and Weber and Morris' intraparticle diffusion models based on Eqs. (2–4).

$$\ln(q_e - q_t) = lnq_e - kt \quad (2)$$

$$\frac{t}{q_t} = \frac{1}{k_2 q_e^2} + \frac{t}{q_e} \quad (3)$$

$$q_t = k_i t^{0.5} + C \quad (4)$$

where q_t (mg/g) is the amount of adsorbed metal ions at time t, q_e (mg/g) is the adsorption capacity, k (min^{-1}) is the first-order rate constant, k_2 (g/mg min) is the second-order rate constant of adsorption (min^{-1}), and k_i ($mg\,min^{1/2}$/g) and C are the kinetic constant and constant of the intra-particle diffusion model, respectively [38,39].

The R^2 values of the calculated parameters listed in Table 1 show that the pseudo-second-order kinetic model is the best fit for adsorption by γ-Fe_2O_3/Mt and γ-Fe_2O_3. Meanwhile, adsorption by Mt follows the pseudo-first-order kinetics. From the Q_e data from all adsorbents, it can also be seen that adsorption capacity is in following order: γ-Fe_2O_3/Mt > Mt > γ-Fe_2O_3, suggesting the provided surface active for adsorption by Mt as support. A synergistic effect of the increasing adsorption capacity is in consistence with the increasing specific surface area. The plots of pseudo-second-order from the adsorption using γ-Fe_2O_3/Mt at varied concentrations are presented in Fig. 7d. These data suggest that adsorption by γ-Fe_2O_3/Mt adsorbents is largely controlled by the chemisorption mechanism rather than mass transport. This is in contrast to the adsorption by Mt, for which the best fit is pseudo-first-order kinetics. Moreover, the adsorption capacity was enhanced either by the pseudo-first- or pseudo-second-order kinetic model. Based on these kinetic parameters, the chemical interaction caused by the γ-Fe_2O_3 dispersion in the Mt surface can be described.

The details of the adsorbate-adsorbent interaction were evaluated by determining the adsorption isotherm using the Freundlich and Langmuir isotherms. The equations used for the Freundlich and Langmuir models were as follows (Eqs. 4 and 5):

$$q_e = K_F C_e^{1/n} \quad (4)$$

$$q_e = \frac{q_m K_L C_e}{1 + K_L C_e} \quad (5)$$

where q_e and q_m (mg/g) are the adsorption capacities of the adsorbent at the equilibrium and maximum values, respectively; Ce (mg/L) is the concentration of the adsorbate in equilibrium; K_F and n are the Freundlich constants related to the adsorption–desorption equilibrium, K_L (L/mg) is the Langmuir constant related to the energy of adsorption and adsorption intensity [40,41].

The R_L parameter from the Langmuir isotherm is represented as follows (Eq. 6):

$$R_L = \frac{1}{1 + K_L q_m} \quad (6)$$

Table 2 lists the calculated isotherm parameters, and the fittest plot is presented in Fig. 7e.

The R^2 values suggest that the Freundlich isotherm model is more feasible than the Langmuir isotherm for adsorption by all tested materials. However, for RhB adsorption by γ-Fe_2O_3/Mt, the R^2 value was higher than that for the Langmuir isotherm. By contrast, adsorption by Mt showed a better fit for the Langmuir isotherm. The K_F and K_L values showed significant improvements in adsorption capability. Both constants from γ-Fe_2O_3/Mt were twice the values from Mt, while the

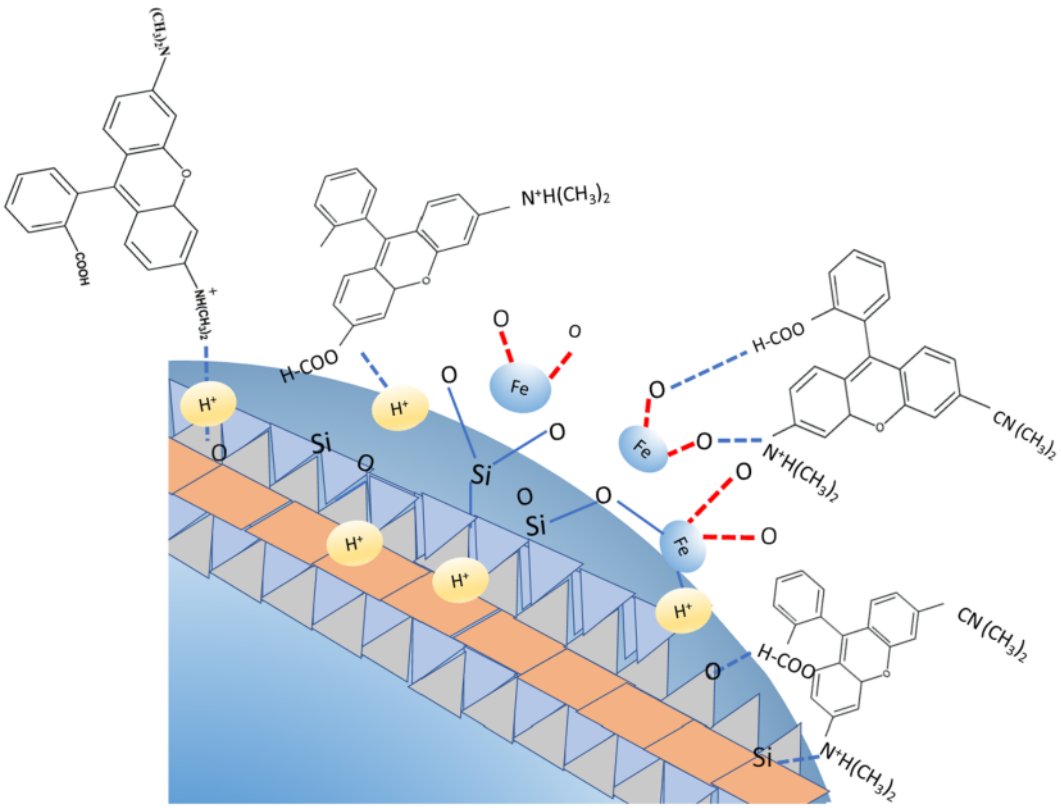

Fig. 8. Schematic diagram of RhB adsorption mechanism by γ-Fe_2O_3 /Mt.

Brunauer-Emmett-Teller (BET) surface area of γ-Fe_2O_3/Mt was not higher than twice the BET surface area value. This can be ascribed to the role of dispersed nanoparticles in adsorption-active sites [42]. The enhanced hydrophilicity, along with the presence of abundant negative functional surface groups (−O and − OH), is the most possible explanation for the rapid adsorption of RhB. This assumption is justified by the low zeta potential of γ-Fe_2O_3/Mt (pH 5.8) compared with that of Mt (pH 6.8). A schematic representation of the mechanism can be seen in Fig. 8.

3.3. Photocatalytic activity study

The photocatalytic activity of γ-Fe_2O_3/Mt is presented by the kinetics of RhB removal at different initial concentrations (Fig. 9a). For each experiment, a mixture of dye solution and photocatalyst powder was first kept in the dark for 15 min with constant stirring. The stirring in the dark was aimed to get adsorption equilibrium prior photocatalysis. The plot shows that the degradation efficiency reached greater than 96% at 30 min and 99% at 60 min at all concentrations. The comparison of DE values by photocatalysis over γ-Fe_2O_3/Mt and γ-Fe_2O_3 presented in Fig. 9b suggest the similar DE at low RhB concentration (2–10 ppm), but at increasing concentration γ-Fe_2O_3/Mt was superior respect to γ-Fe_2O_3. The higher degradation is attributed to the contributing adsorption mechanism which is more dominant in γ-Fe_2O_3/Mt. The contribution adsorption in photocatalytic mechanism was also reported in the use of BiOBr, Fe_3O_4@MoS_2, and Fe(III)/montmorillonite [43–45]. The DE values indicated that the γ-Fe_2O_3/Mt had high efficiency, as also demonstrated in the comparison with the DE values obtained from other similar works listed in Table 3. The DE value obtained in this work was higher than that of γ-Fe_2O_3/SiO_2, which was 95% at the same duration of 30 min, and that of Ag–AgI/Fe_3O_4@SiO_2, which was 95% at 1 h of treatment [46–51].

3.4. Degradation mechanism

The identification of the degradation mechanism in photocatalysis in comparison with the adsorption mechanism was performed using UV–visible spectrophotometry and liquid chromatography coupled to mass spectrometry (LCMS) analysis. The UV–visible spectra in Fig. 9b and 9c represent a significant difference among the spectral changes obtained by adsorption and the photocatalysis mechanism. Adsorption produced reduced absorbance spectra along with prolonged treatment time. From the photocatalysis treatment, not only reduced absorbance but also the red shift of the characteristic peak of 556 nm was found. The red shift is characteristic of deethylation and decarboxylation. This is also confirmed by the LCMS analysis presented in Fig. 10. The LC analysis of the treated solution revealed some other peaks as proof of the degradation products (Fig. 10a). Besides the other peaks found in the treated solution from the LC analysis (Fig. 10b), the treated solutions exhibited fractions with m/z values of 359, 331, 181, 168, 146, and 128

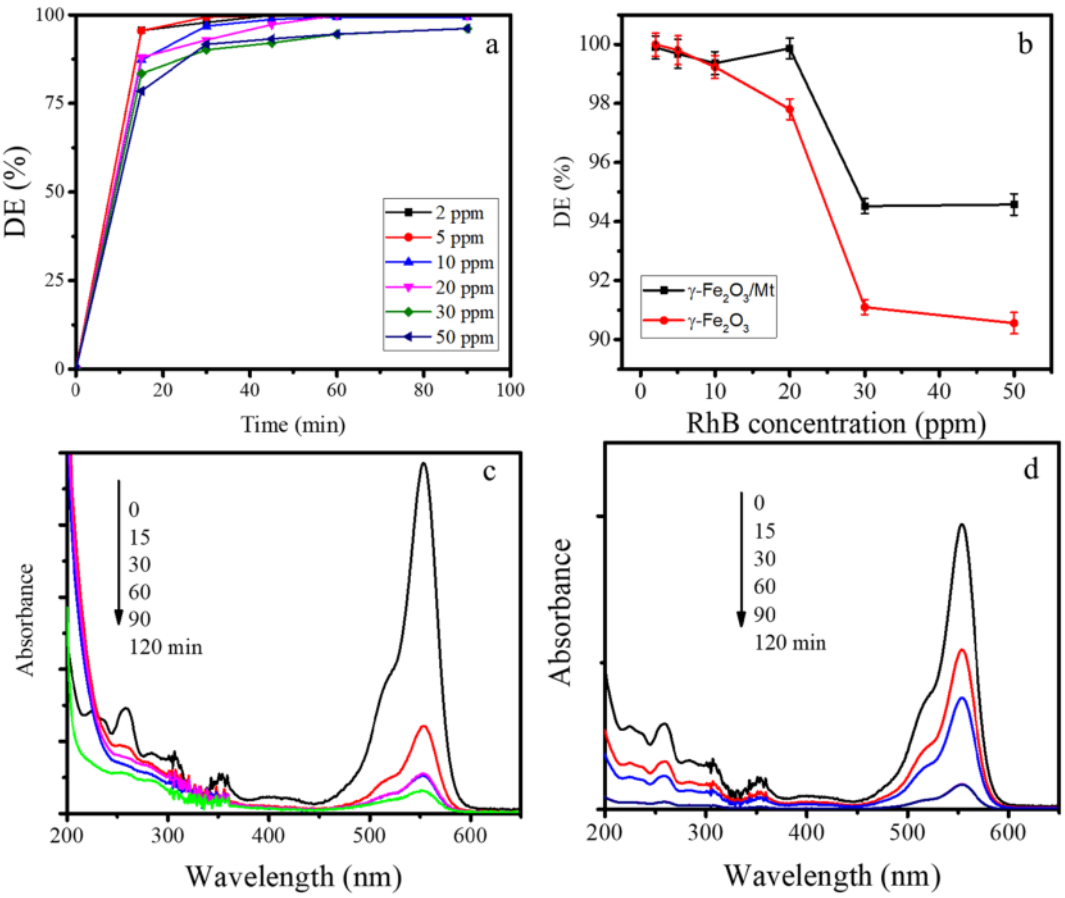

Fig. 9. (a) DE of photocatalytic degradation using γ-Fe_2O_3 /Mt at varied concentration (b) Comparison on DE by photocatalytic degradation using γ-Fe_2O_3 /Mt and γ-Fe_2O_3 (c) UV–Visible spectral change by photocatalytic mechanism (d) UV–Visible spectral change by adsorption mechanism.

Table 3
RhB removal by various materials.

Material	DE (%)	Remark	Reference
αFe_2O_3 NPs	73 at 1 h	Particle size of αFe_2O_3 is ranging at 48–55 nm with the band gap energy of 2.14 eV	[39]
γ-Fe_2O_3/SiO_2	95 at 30 min	The DE achieved by the photocatalyst dose of 0.8 g/L, silica was derived from rice husk ash	[40]
$BaTiO_3$/MnO_2	70 at 3 h	photodegradation of RhB in the presence of MnO2 -modified BTO ceramics followed a pseudo-first order model a	[41]
Ag–AgI/ Fe_3O_4@SiO_2	95 at 1 h	The light source was a 250 W lamp, photocatalyst dosage of 0.1 g/L	[42]
Cu–Fe_3O_4 magnetic nanoparticles	92.8 at 1 h	The optimum degradation was achieved at pH ~7 and 25 °C and the rate constant of about 0.0256 min^{-1}.	[43]
$NiMn_2O4$ nanoparticles	98 at 80 min	The photocatalyst has the band gap energy of 3.0 eV	[44]

as degradation products. These spectra elucidate that the possible degradation mechanism can be described using the following scheme (Fig. 11):

These analyses are similar to the identification of RhB degradation over other TiO_2-supported activated carbons and SnO_2/Mt [17].

To further determine how reactive species induce the degradation mechanism, hole and hydroxy radical scavengers were added to the photocatalytic system. To this, isopropanol (IPR) was added as the hydroxy radical scavenger, while the EDTA was added as a hole scavenger. The effect of the addition to the degradation rate is depicted in the kinetic plots and the calculated initial rates presented in Fig. 12. Fig. 12a and Fig. 12b show that the photodegradation rate was increased with the addition of EDTA and decreased with the addition of IPR. In order to reduce the interpretation on decreasing concentration caused by adsorption pathway, the test on scavenger addition under light illumination was performed by previously treated by adsorption under dark condition. The proof that the degradation mechanism occurred by varied treatment, HPLC analysis was performed with the chromatogram presented in Fig. 13. The chromatogram of initial RhB shows the single dominant peak at 6.8 min as identity of RhB molecule. After was treated

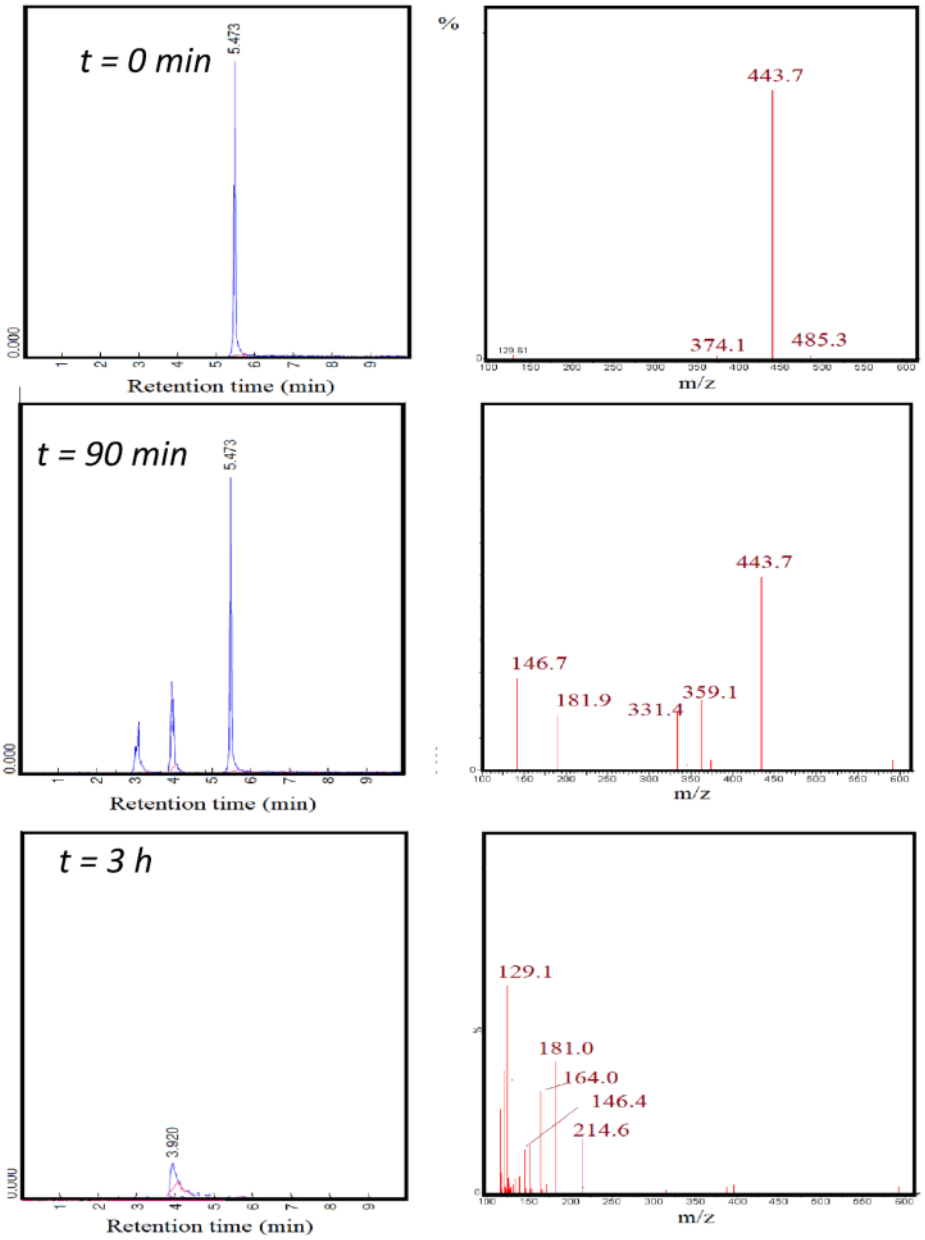

Fig. 10. LCMS profile of initial and treated solutions.

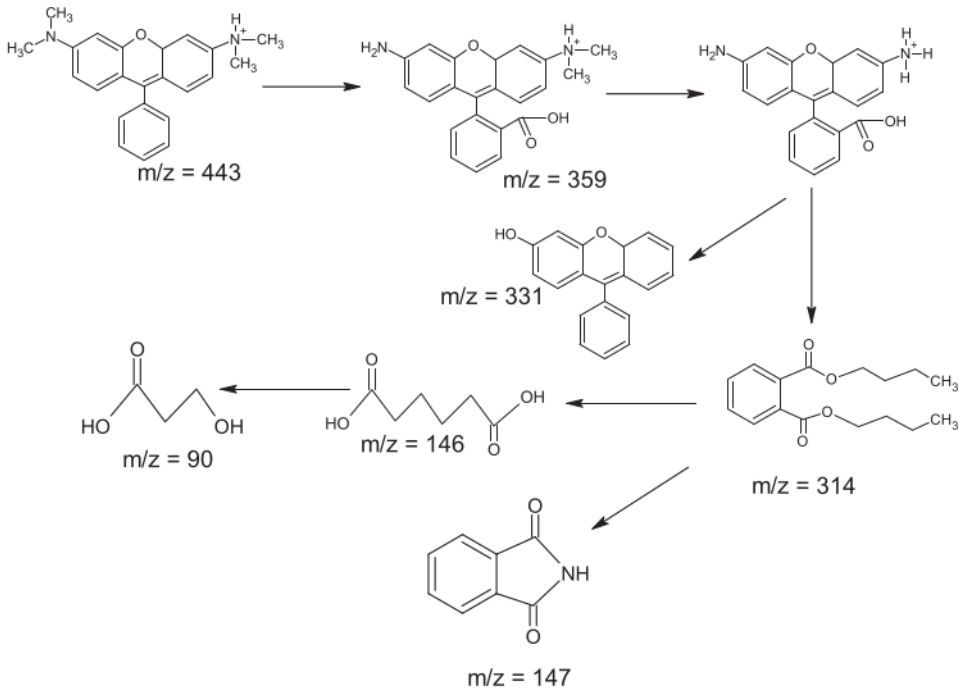

Fig. 11. Proposed mechanism of RhB degradation by photooxidation using γ-Fe_2O_3 /Mt.

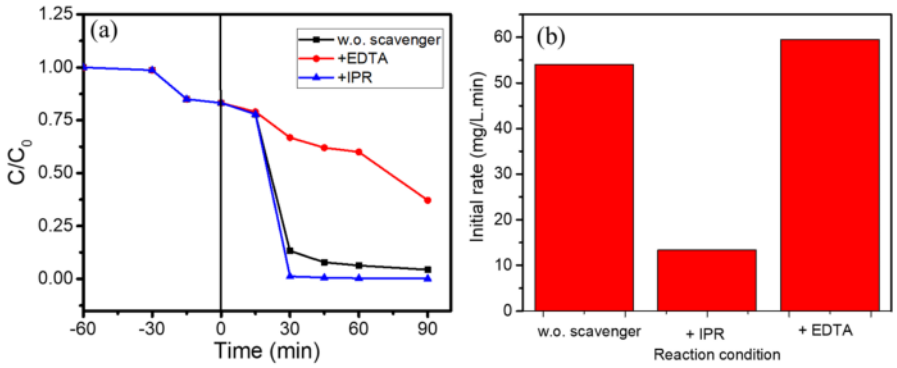

Fig. 12. (a). DE RhB (b) Initial rate of degradation using γ-Fe_2O_3 /Mt with and without scavenger.

by varied condition, the chromatograms exhibit other peaks at less retention time, associated with smallest molecular weight. It suggest that there was degradation of RhB structure as shown by other peaks in all varied treated solutions for 30 min. The slower degradation rate by IPR addition was confirmed by the higher concentration of rest RhB in the solution. Contrarily, the faster degradation by EDTA addition was expressed by less intense RhB peak, along with some more intensive peaks of degradation products. This phenomenon revealed the role of the promoted separation of electron-hole pairs related directly to the increased lifetime of electron-hole pairs. In addition, the trapping hydroxy radicals by IPR inhibited the propagation reaction owing to their consumption in further oxidation process toward RhB. These results imply that the radicals were the predominant reactive species for the photocatalytic degradation of RhB. A similar effect was reported for the photocatalytic activity of Fe_2O_3 nanoparticles [52] and $BiFeO_3$ nanostructures [53].

3.5. Reusability study

Examination of reusability is an important evaluation for a photocatalyst to be applied on an industrial scale. The experiments were conducted in five cycles based on the initial rate and DE achieved at 30 min. The photocatalyst was recycled by filtering, washing using n-hexane, and calcined for 200 °C after the completion of each cycle. The easily separable property of the material is related to the magnetism feature measured using the VSM analysis presented in Fig. 14a. The magnetism plot shows that the γ-Fe_2O_3/Mt demonstrates specific magnetic saturation magnitudes of 22.7 emu/g. This value is less than the magnetism of γ-Fe_2O_3 NPs prepared from various experimental methods, which ranged from 60 to 70 emu/g, representing the influence of the non-magnetic properties of clay support. However, magnetism is still applicable for magnetic attraction for easy separation with high recoverability. The bar chart depicted in Fig. 14b shows that the

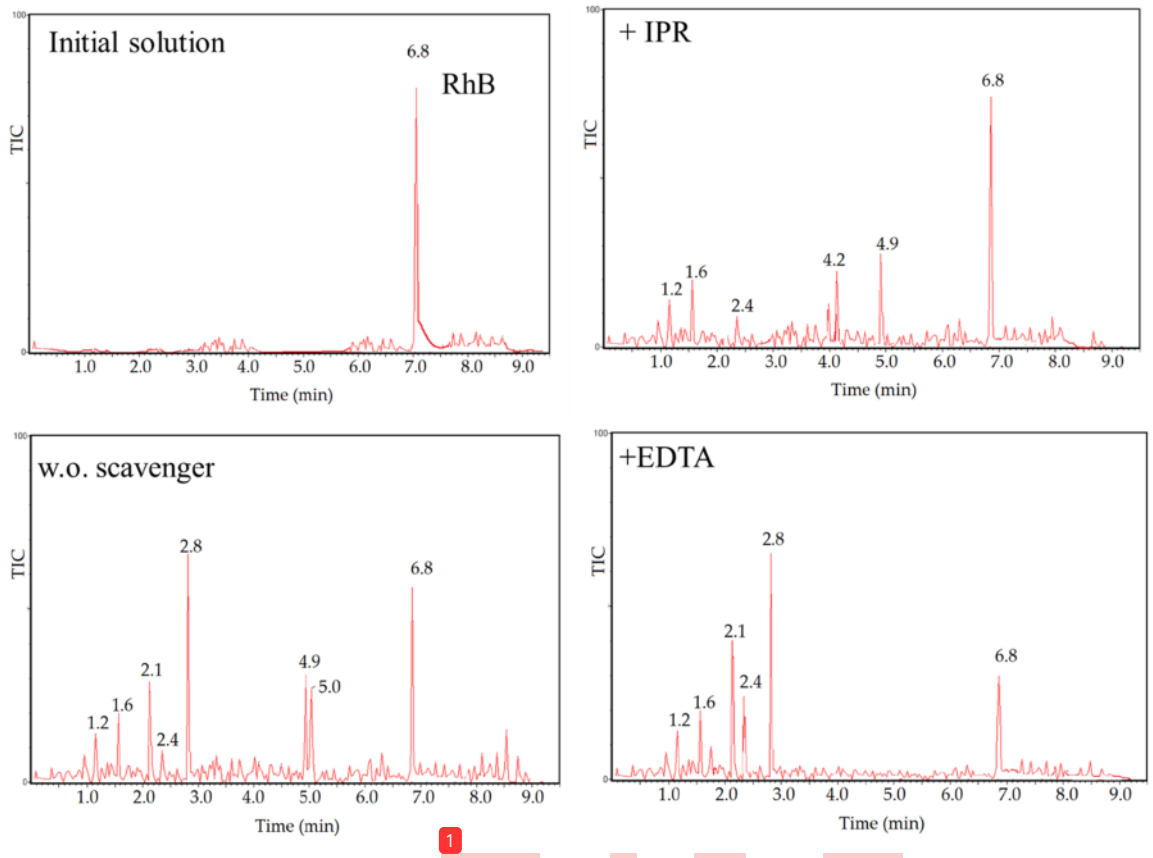

Fig. 13. Chromatograms of initial RhB solution and varied treated solutions for 30 min.

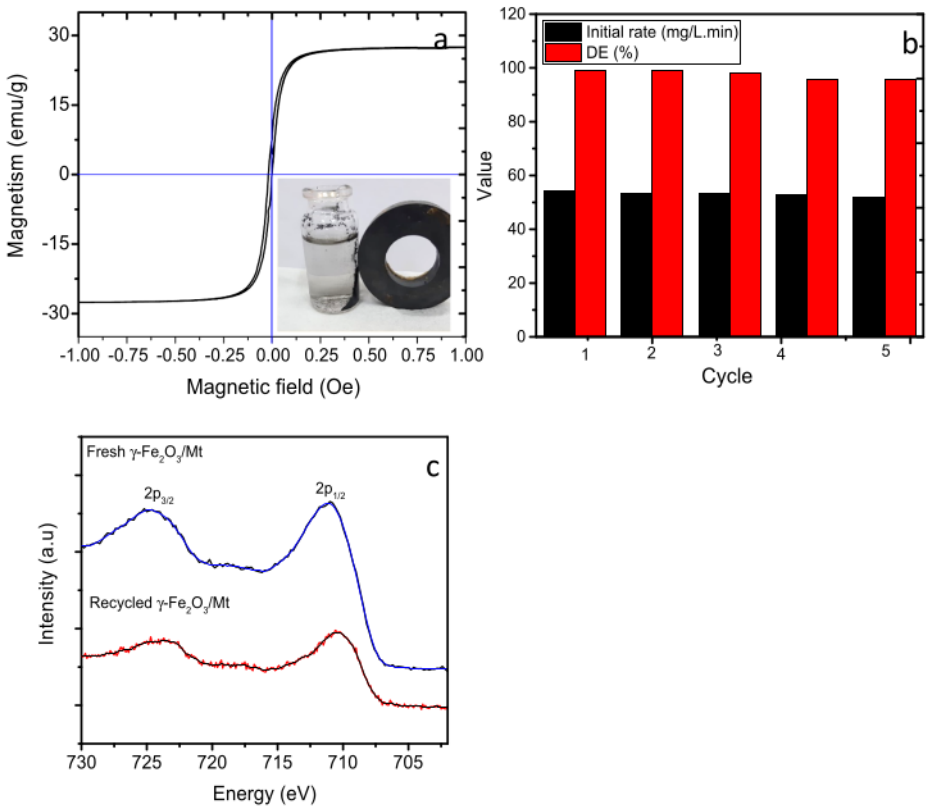

Fig. 14. (a). Magnetism curve of γ-Fe_2O_3 /Mt (b) Initial rate and DE RhB degradation using γ-Fe_2O_3 /Mt at various cycles (c). Comparison on XPS Fe 2p spectrum fresh and recycled γ-Fe_2O_3 /Mt.

photocatalytic activity achieved was quite stable, as confirmed by the maintained DE at approximately 97–99% and the reduction of the initial rate to $\leq$ 10%. In addition, the stability of the photocatalyst was also monitored by XRD measurement and XPS of the reused photocatalyst. The spectra of Fe 2p presented in Fig. 14 c suggest the insignificant change of the material. No other reflection was identified in the recycled photocatalyst, and no other peaks in the XPS profile were observed, confirming that the single-ion species of Fe^{3+} were maintained.

Finally, the γ-Fe_2O_3/Mt nanocomposite exhibited excellent properties in terms of visible-light activity, easy magnetic separation, stability, and reusability, making it practically applicable in dye photo-oxidation. Mt is an abundant, low-cost, naturally occurring material that will contribute to the economic value of nanocomposites to be further developed.

4. Conclusion

A nanocomposite of γ-Fe_2O_3/Mt was successfully prepared using a hydrothermal method. The nanocomposite demonstrated excellent features as an adsorbent and photocatalyst for RhB removal. The homogeneous dispersion of the single-phase γ-Fe_2O_3 nanoparticles in the Mt structure contributed to the enhanced dye-surface interaction, as shown by the significant improvement in adsorption capability. The narrow band-gap energy of 3.2 eV is fit visible light and attractivity to magnetic force provide the benefits of a low-cost and easy handling photocatalytic system. In addition, the nanocomposite showed a magnetically separable performance for complete recovery after use. The stability of the nanocomposite, proven by the relatively unchanged phase after use for many cycles, greatly promotes its potential practical application for the removal of dye pollutants from wastewater.

Declaration of Competing Interest

The authors declare that they have no known competing financial interests or personal relationships that could have appeared to influence the work reported in this paper.

Acknowledgments

The authors gratefully acknowledge the financial support from the Kementrian Riset-Badan Riset Nasional, Republic of Indonesia via World Class Research Grant, under contract No. 018/DirDPPM/70/DPPM/WCR/EMDIKBUDRISTEK/VII/2021. The authors also thank the Bunseki Analysis Center of Gifu University for allowing access to XPS analysis.

References

[1] K.M. Reza, A. Kurny, F. Gulshan, Parameters affecting the photocatalytic degradation of dyes using TiO2: a review, Appl. Water Sci. 7 (4) (2017) 1569–1578, https://doi.org/10.1007/s13201-015-0367-y.
[2] T. Shindhal, P. Rakholiya, S. Varjani, A. Pandey, H.H. Ngo, W. Guo, H.Y. Ng, M. J. Taherzadeh, A critical review on advances in the practices and perspectives for the treatment of dye industry wastewater, Bioengineerd. 12 (1) (2021) 70–87.
[3] R. Kant, Textile dyeing industry an environmental hazard, Nat. Sci. 04 (01) (2012) 22–26, https://doi.org/10.4236/ns.2012.41004.
[4] Y. Deng, R. Zhao, Advanced Oxidation Processes (AOPs) in Wastewater Treatment, Curr. Pollut. Reports. 1 (3) (2015) 167–176, https://doi.org/10.1007/s40726-015-0015-z.

[5] M.A. Johar, R.A. Afzal, A.A. Alazba, U. Manzoor, Photocatalysis and Bandgap Engineering Using ZnO Nanocomposites, Photocatalysis and Bandgap Engineering Using ZnO Nanocomposites 2015 (2015) 1–22.

[6] M. He, D. Li, D. Jiang, M. Chen, Magnetically separable γ-Fe 2O 3@SiO 2@Ce-doped TiO 2 core-shell nanocomposites: Fabrication and visible-light-driven photocatalytic activity, J. Solid State Chem. 192 (2012) 139–143, https://doi.org/10.1016/j.jssc.2012.04.004.

[7] Y. Chen, Z. Xiang, D. Wang, J. Kang, H. Qi, Effective photocatalytic degradation and physical adsorption of methylene blue using cellulose/GO/TiO2hydrogels, RSC Adv. 10 (40) (2020) 23936–23943.

[8] W. Liu, T. He, Y. Wang, G. Ning, Z. Xu, X. Chen, X. Hu, Y. Wu, Yunlin Zhao, Synergistic adsorption-photocatalytic degradation effect and norfloxacin mechanism of Zno/ZnS@Bc under UV-light irradiation, Sci. Rep. 10 (2020) 11903.

[9] N.H. Abdullah, K. Shameli, E.C. Abdullah, L.C. Abdullah, Solid matrices for fabrication of magnetic iron oxide nanocomposites: Synthesis, properties, and application for the adsorption of heavy metal ions and dyes, Compos. Part B Eng. 162 (2019) 538–568, https://doi.org/10.1016/j.compositesb.2018.12.075.

[10] Y. Tu, Z. Peng, P. Xu, H. Lin, X. Wu, L. Yang, J. Huang, Characterization and Application of Magnetic Biochars from Corn Stalk by Pyrolysis and Hydrothermal Treatment, BioResources. 12 (2017) 1077–1089, https://doi.org/10.15376/biores.12.1.1077-1089.

[11] A. Sarwar, J. Wang, M.S. Khan, U. Farooq, N. Riaz, A. Nazir, Q. Mahmood, A. Hashem, A.-B. Al-Arjani, A.A. Alqarawi, E.F. Abd_Allah, Iron oxide (Fe3o4)-supported sio2 magnetic nanocomposites for efficient adsorption of fluoride from drinking water: Synthesis, characterization, and adsorption isotherm analysis, Water (Switzerland) 13 (11) (2021) 1514, https://doi.org/10.3390/w13111514.

[12] S.Y. An, I.B. Shim, C.S. Kim, Easy synthesis and characterization of γ- Fe2 O3 nanoparticles for biomedical applications, J. Appl. Phys. 97 (2005) 11–14, https://doi.org/10.1063/1.1851919.

[13] G. Fadillah, S.P. Yudha, S. Sagadevan, I.s. Fatimah, O. Muraza, Magnetic iron oxide/clay nanocomposites for adsorption and catalytic oxidation in water treatment applications, Open Chem. 18 (1) (2020) 1148–1166, https://doi.org/10.1515/chem-2020-0159.

[14] R. Zhang, Investigation of Magnetic Modified Clay Nano-adsorbents in Removing Micro-pollution from potable water, in: Int. Conf. Biol. Chem. Environ. Sci., 2016: pp. 6–11. https://doi.org/10.15242/iicbe.c0816201.

[15] T. Szabó, A. Bakandritsos, V. Tzitzios, S. Papp, L. Korösi, G. Galbács, K. Musabekov, D. Bolatova, D. Petridis, I. Dékány, Magnetic iron oxide/clay composites: Effect of the layer silicate support on the microstructure and phase formation of magnetic nanoparticles, Nanotechnology. 18 (28) (2007) 285602, https://doi.org/10.1088/0957-4484/18/28/285602.

[16] S.A. Jayanthi, D.M.G.T. Nathan, J. Jayashainy, P. Sagayaraj, A novel hydrothermal approach for synthesizing α-Fe2O3, γ-Fe2O3 and Fe3O4 mesoporous magnetic nanoparticles, Mater. Chem. Phys. 162 (2015) 316–325, https://doi.org/10.1016/j.matchemphys.2015.05.073.

[17] I.s. Fatimah, D. Rubiyanto, I. Sahroni, R.S. Putra, R. Nurillahi, J. Nugraha, Physicochemical characteristics and photocatalytic performance of Tin oxide/montmorillonite nanocomposites at various Sn/montmorillonite molar to mass ratios, Appl. Clay Sci. 193 (2020) 105671, https://doi.org/10.1016/j.clay.2020.105671.

[18] R. Mahajan, S. Suriyanarayanan, I.A. Nicholls, Improved solvothermal synthesis of γ-Fe2O3 magnetic nanoparticles for SiO2 coating, Nanomaterials. 11 (8) (2021) 1889, https://doi.org/10.3390/nano11081889.

[19] T.S. Kakuta, Abe, Photocatalysis for water oxidation by Fe2O3 nanoparticles embedded in clay compound: correlation between its polymorphs and their photocatalytic activities, J. Matter. Sci. 44 (2009) 2890–2898.

[20] Z. Tashrifi, S. Bahadorikhalili, H. Lijan, S. Ansari, H. Hamedifar, M. Mahdavi, Synthesis and characterization of γ-Fe2O3@SiO2-(CH2)3-PDTC-Pd magnetic nanoparticles: A new and highly active catalyst for the Heck/Sonogashira coupling reactions, New J. Chem. 43 (23) (2019) 8930–8938.

[21] S. Sundar, G. Venkatachalam, S. Kwon, Sol-gel mediated greener synthesis of γ-Fe2O3 nanostructures for the selective and sensitive determination of uric acid and dopamine, Catalysts. 8 (11) (2018) 512, https://doi.org/10.3390/catal8110512.

[22] Z. Chen, Y. Ma, B. Geng, M. Wang, X. Sun, Photocatalytic performance and magnetic separation of TiO2-functionalized γ-Fe2O3, Fe, and Fe/Fe2O3magnetic particles, J. Alloys Compd. 700 (2017) 113–121, https://doi.org/10.1016/j.jallcom.2017.01.045.

[23] I. Kazeminezhad, S. Mosivand, Phase transition of electrooxidized Fe3O4 to γ and α-Fe2O3 nanoparticles using sintering treatment, Acta Phys. Pol. A. 125 (2014) 1210–1214, https://doi.org/10.12693/APhysPolA.125.1210.

[24] P.S. Bagus, C.J. Nelin, C.R. Brundle, N. Lahiri, E.S. Ilton, K.M. Rosso, Analysis of the Fe 2p XPS for hematite α Fe2O3: Consequences of covalent bonding and orbital splittings on multiplet splittings, J. Chem. Phys. 152 (1) (2020) 014704, https://doi.org/10.1063/1.5135595.

[25] R.A. Bepari, P. Bharali, B.K. Das, Controlled synthesis of α- and γ-Fe2O3 nanoparticles via thermolysis of PVA gels and studies on α-Fe2O3 catalyzed styrene epoxidation, J. Saudi Chem. Soc. 21 (2017) S170–S178, https://doi.org/10.1016/j.jscs.2013.12.010.

[26] X. Jiang, J. Nie, L. Bian, F. Dong, M. Song, Y.i. He, H. He, Z. Zheng, T. Huo, B. Li, N. Belzile, S. Sun, H. Zou, Competitive Adsorption of Uranyl and Toxic Trace Metal Ions at MFe2O4-montmorillonite (M = Mn, Fe, Zn Co, or Ni) Interfaces, Clays Clay Miner. 67 (4) (2019) 291–305, https://doi.org/10.1007/s42860-019-00028-x.

[27] E. Paparazzo, On the quantitative XPS analysis of Fe2O3 and Fe1-xO oxides, J. Electron Spectros. Relat. Phenomena. 154 (1-2) (2006) 38–40, https://doi.org/10.1016/j.elspec.2006.09.004.

[28] Y.Q. Cao, T.Q. Zi, X.R. Zhao, C. Liu, Q. Ren, J. Bin Fang, W.M. Li, A.D. Li, Enhanced visible light photocatalytic activity of Fe2O3 modified TiO2 prepared by atomic layer deposition, Sci. Rep. 10 (2020) 1–10, https://doi.org/10.1038/s41598-020-70352-z.

[29] S.N. Ahmed, A. Inam, W. Haider, γ-Fe2O3 photocatalyst immobilized on a porous Ni substrate for recyclable solar photocatalysis, J. Nanoparticle Res. 21 (11) (2019), https://doi.org/10.1007/s11051-019-4663-6.

[30] J. Lee, S.-Y. Kwak, Mn-Doped Maghemite (γ-Fe2O3) from Metal-Organic Framework Accompanying Redox Reaction in a Bimetallic System: The Structural Phase Transitions and Catalytic Activity toward NOx Removal, ACS Omega. 3 (3) (2018) 2634–2640, https://doi.org/10.1021/acsomega.7b0186510.1021/acsomega.7b01865.s001.

[31] N. Ferroudj, J. Nzimoto, A. Davidson, D. Talbot, E. Briot, V. Dupuis, A. Bée, M. S. Medjram, S. Abramson, Maghemite nanoparticles and maghemite/silica nanocomposite microspheres as magnetic Fenton catalysts for the removal of water pollutants, Appl. Catal. B Environ. 136–137 (2013) 9–18, https://doi.org/10.1016/j.apcatb.2013.01.046.

[32] M. Jin, M. Long, H. Su, Y. Pan, Q. Zhang, J. Wang, B. Zhou, Y. Zhang, Magnetically separable maghemite/montmorillonite composite as an efficient heterogeneous Fenton-like catalyst for phenol degradation, Environ. Sci. Pollut. Res. 24 (2) (2017) 1926–1937, https://doi.org/10.1007/s11356-016-7866-8.

[33] S. Singh, G. Hitkari, G. Pandey, Effect of annealing temperature on structural, optical and photocatalytic properties of α-Fe 2 O 3 nanostructures, Inorg. Nano-Metal Chem. 48 (10) (2018) 477–485, https://doi.org/10.1080/24701556.2019.1571511.

[34] M. Valášková, J. Tokarský, J. Pavlovský, T. Prostějovský, K. Kočí, α-Fe2O3 nanoparticles/vermiculite clay material: Structural, optical and photocatalytic properties, Materials (Basel). 12 (2019) 1–16, https://doi.org/10.3390/ma12111880.

[35] S. Guo, G. Zhang, J. Wang, Photo-Fenton degradation of rhodamine B using Fe2O3-Kaolin as heterogeneous catalyst: Characterization, process optimization and mechanism, J. Colloid Interface Sci. 433 (2014) 1–8, https://doi.org/10.1016/j.jcis.2014.07.017.

[36] D. Cao, H. Li, L. Pan, J. Li, X. Wang, P. Jing, X. Cheng, W. Wang, J. Wang, Q. Liu, High saturation magnetization of γ 3-Fe2 O3 nano-particles by a facile one-step synthesis approach, Sci. Rep. 6 (2016) 1–9, https://doi.org/10.1038/srep32360.

[37] C.B. Vidal, A.B. dos Santos, R.F. do Nascimento, T.J. Bandosz, Reactive adsorption of pharmaceuticals on tin oxide pillared montmorillonite: Effect of visible light exposure, Chem. Eng. J. 259 (2015) 865–875, https://doi.org/10.1016/j.cej.2014.07.079.

[38] C. Zou, J. Liang, W. Jiang, Y. Guan, Y. Zhang, Adsorption behavior of magnetic bentonite for removing Hg(II) from aqueous solutions, RSC Adv. 8 (2018) 27587–27595, https://doi.org/10.1039/c8ra05247f.

[39] W. Lee, S. Yoon, J.K. Choe, M. Lee, Y. Choi, Anionic surfactant modification of activated carbon for enhancing adsorption of ammonium ion from aqueous solution, Sci. Total Environ. 639 (2018) 1432–1439, https://doi.org/10.1016/j.scitotenv.2018.05.250.

[40] A.O. Dada, A.P. Olalekan, A.M. Olatunya, O. Dada, Langmuir, Freundlich, Temkin and Dubinin-Radushkevich Isotherms Studies of Equilibrium Sorption of Zn 2+ Unto Phosphoric Acid Modified Rice Husk, IOSR J. Appl. Chem. 3 (2012) 38–45, https://doi.org/10.9790/5736-0313845.

[41] S. Khezrianjoo, H. Revanasiddappa, Langmuir-Hinshelwood Kinetic Expression for the Photocatalytic Degradation of Metanil Yellow Aqueous Solutions by ZnO Catalyst, Chem. Sci. J. 2012 (2012) 85. http://astonjournals.com/csj.

[42] L.D.T. Camara, A.J. Silva Neto, Modeling of the Kinetics of Salycilic Acid Adsorption in Polymeric and Activated Charcoal Adsorbents, Ciencia. 7 (2008) 49–54.

[43] D.H. Bachir, H. Boutoumi, H. Khalaf, P. Eloy, J. Schnee, E.M. Gaigneaux, Influence of operational parameters on photocatalytic degradation of linuron in aqueous TiO2 pillared montmorillonite suspension, Bull. Chem. React. Eng. Catal. 16 (2021) 673–685, https://doi.org/10.9767/BCREC.16.3.11108.673-685.

[44] L.i. Zhang, C. Chuaicham, V. Balakumar, B. Ohtani, K. Sasaki, Fabrication of Adsorbed Fe(III) and Structurally Doped Fe(III) in Montmorillonite/TiO2 Composite for Photocatalytic Degradation of Phenol, Minerals 11 (12) (2021) 1381, https://doi.org/10.3390/min11121381.

[45] C. Zhou, W. Liu, H. Li, M. Yang, Z. Yang, Separable magnetic Fe3O4@MoS2 composite for adsorption and Piezo-Catalytic degradation of dye, Catalysts. (2016) 1–23.

[46] M. Mahadik, S. Shinde, V. Mohite, S. Kumbhar, K. Rajpure, A. Moholkar, J. Kim, C. Bhosale, Photoelectrocatalytic oxidation of Rhodamine B with sprayed α-Fe2O3 photocatalyst, Mater. Express. 3 (2013) 247–255, https://doi.org/10.1166/mex.2013.1120.

[47] I.s. Fatimah, S. Fadhilah, Y. Sherlita, A. Mawardani, γ-Fe2O3 Nanoparticles Immobilized in SiO2 Aerogel Synthesized from Rice Husk Ash for Photo-Fenton Like Degradation of Rhodamine B, Rasayan J. Chem. 11 (2) (2018) 544–553.
[48] I. Kuźniarska-Biernacka, B. Garbarz-Glos, E. Skiba, W. Maniukiewicz, W. Bąk, M. Antonova, S.L.H. Rebelo, C. Freire, Evaluation of rhodamine b photocatalytic degradation over batio3-mno2 ceramic materials, Materials (Basel). 14 (12) (2021) 3152, https://doi.org/10.3390/ma14123152.
[49] J.-F. Guo, B. Ma, A. Yin, K. Fan, W.-L. Dai, Photodegradation of rhodamine B and 4-chlorophenol using plasmonic photocatalyst of Ag-AgI/Fe3O4@SiO2 magnetic nanoparticle under visible light irradiation, Appl. Catal. B Environ. 101 (3-4) (2011) 580–586, https://doi.org/10.1016/j.apcatb.2010.10.032.
[50] W. Du, R. Huang, X. Huang, R. Chen, F. Chen, Copper-promoted heterogeneous Fenton-like oxidation of Rhodamine B over Fe3O4 magnetic nanocatalysts at mild conditions, Environ. Sci. Pollut. Res. 28 (16) (2021) 19959–19968, https://doi.org/10.1007/s11356-020-12264-z.
[51] F. Sedighi, A. Sobhani-Nasab, M. Behpour, M. Rahimi-Nasrabadi, Photocatalytic Degradation of Rhodamine B, and Phenol Red Dyes using NiMn2O4 Nanoparticles Prepared by a New Approach, J. Nanostructures. 9 (2019) 258–267, https://doi.org/10.22052/JNS.2019.02.008.
[52] A. Kusior, K. Michalec, P. Jelen, M. Radecka, Shaped Fe 2 O 3 nanoparticles – Synthesis and enhanced photocatalytic degradation towards RhB, Appl. Surf. Sci. 476 (2019) 342–352, https://doi.org/10.1016/j.apsusc.2018.12.113.
[53] F. Mushtaq, X. Chen, M. Hoop, H. Torlakcik, E. Pellicer, J. Sort, C. Gattinoni, B. J. Nelson, S. Pané, Piezoelectrically Enhanced Photocatalysis with BiFeO3 Nanostructures for Efficient Water Remediation, IScience. 4 (2018) 236–246, https://doi.org/10.1016/j.isci.2018.06.003.

Mechanistic insight into the adsorption and photocatalytic activity of a magnetically separable

ORIGINALITY REPORT

12%	9%	7%	0%
SIMILARITY INDEX	INTERNET SOURCES	PUBLICATIONS	STUDENT PAPERS

PRIMARY SOURCES

1	www.degruyter.com Internet Source	3%
2	www.researchgate.net Internet Source	3%
3	biointerfaceresearch.com Internet Source	2%
4	Fitriana Harjati, Putwi Widya Citradewi, Gani Purwiandono, Is Fatimah. "Green synthesis of hematite/TUD-1 nanocomposite as efficient photocatalyst for bromophenol blue and methyl violet degradation", Arabian Journal of Chemistry, 2020 Publication	2%
5	Suresh Sagadevan, Solhe F. Alshahateet, J. Anita Lett, Is Fatimah et al. "Highly efficient photocatalytic degradation of methylene blue dye over Ag2O nanoparticles under solar light irradiation", Inorganic Chemistry Communications, 2022 Publication	2%

Exclude quotes	On	Exclude matches	< 2%
Exclude bibliography	On		